Terrestrial LiDAR Survey and Morphological Analysis to Identify Infiltration Properties in the Tamala Limestone, Western Australia

Kashif Mahmud, Gregoire Mariethoz, Pauline C. Treble, and Andy Baker

Abstract—Caves are an ideal observatory of infiltration water in karstified limestone, and the application of remote sensing techniques can bring new insights toward flow patterns and processes. We present an exhaustive characterization of Golgotha Cave in SW Western Australia, based on a light detection and ranging (LiDAR) measurement campaign. The cave is developed in Quaternary age aeolianite (dune limestone) and its infiltration waters form speleothems. We collect ground-based LiDAR scans of the cave ceiling at three sites within the cave system. The resulting point-clouds are analyzed using mathematical morphology to determine statistical information on stalactite widths, lengths, and spatial distributions. We establish a relationship between stalactite diameter and length that is in agreement with the platonic ideal of stalactite shape. We relate stalactite density variation with topography of the cave ceiling and variations in hydraulic gradient. From this analysis, it appears that longer stalactites tend to occur in comparatively lower ceiling elevation, which, we hypothesize, represents greater mass of water in the limestone above the roof of the cave. We also investigate the relationship between stalactite distribution and ceiling features such as fractures. We apply this to identify different types of possible flow patterns such as matrix flow and fracture flow. This analysis demonstrates a spatial variability, with one site having linear groups of stalactites and another site mostly dominated by stalactite clusters.

Index Terms—Cave, infiltration, karst, morphology, stalactites.

I. INTRODUCTION

LIGHT detection and ranging (LiDAR) is a commonly used remote sensing technology that allows recording high-resolution surface maps [1]. While it was initially used for mapping particles in the atmosphere [1], today LiDAR has applications in archeology [2], geography [3], geology [4], geomorphology [5], [6], seismology [7], forestry [8]–[11], remote sensing [12], atmospheric physics [13], [14], hydraulic modeling [15], vehicle extraction [16], and contour mapping [17], [18]. It determines the distance to an object or surface by emitting laser pulses and by measuring the properties of the scattered light. It is, therefore, similar to radar technology, but uses visible and infrared light instead of radio waves. The range to an object is determined by measuring the time delay between transmission of a pulse and detection of the reflected signal. Ground-based LiDAR or terrestrial laser scanner (T-LiDAR) has been used since the early 1990s and is capable of producing maps with under 1-cm resolution [1].

Karstic aquifers, formed by the dissolution of soluble rocks, represent 25% of the water resources worldwide [19]. These aquifers contain valuable freshwater resources, but are challenging to exploit and vulnerable due to a strong degree of heterogeneity and connectivity. Karstic formations typically contain conduits that allow the flux or storage of large amounts of water, but also favor quick flow and, therefore, migration of contaminants. To manage the karst resource better, it is important to understand and predict how the water flows in karstified limestone. This includes having an idea of the typical geometry of karst conduits, and how they are connected, as well as a quantification of the relative importance of conduit, fracture, and matrix flow. However, the accurate and complete recording of subsurface karstic features is challenging since it can only be observed in specific caves that are accessible. The walls, floors, and ceilings of a cave typically present irregular surfaces, characterized by flowstones, stalactite, and stalagmites, which can indicate past and present water flowpaths. Reference [20] presents an investigation of the applicability of the Kinect sensor for capturing common karst features in caves and compares the point-cloud with a reference terrestrial laser scan. It suggests that the Kinect-based acquisition is rather suitable for capturing cave surface features such as flowstones. Here, by performing a quantitative analysis of the morphology of karstic features within a cave, we can estimate infiltration water flow processes through fractures and the matrix of the karst system.

T-LiDAR is capable of capturing hundreds of millions of three-dimensional (3-D) points coordinates and its use in geology has been growing [21]–[25]. Once a high-resolution 3-D record of the site features is available, one can visualize, study, and extract two-dimensional (2-D) and 3-D information at

K. Mahmud and A. Baker are with the Connected Waters Initiative Research Centre, University of New South Wales (UNSW) Australia, Sydney, N.S.W. 2052, Australia (e-mail: kashif.mahmud@unsw.edu.au; a.baker@unsw.edu.au).

G. Mariethoz was with the Connected Waters Initiative Research Centre, University of New South Wales (UNSW) Australia, Sydney, N.S.W. 2052, Australia. He is now with the Institute of Earth Surface Dynamics, University of Lausanne, Lausanne CH-1015, Switzerland (e-mail: gregoire.mariethoz@unil.ch).

P. C. Treble is with the Institute for Environmental Research, Australian Nuclear Science and Technology Organisation, Lucas Heights, N.S.W. 2232, Australia (e-mail: ptr@ansto.gov.au).

various scales and from several points of view. Research involving the T-LiDAR technique for karstic model development is still evolving and requires further enhancement, especially concerning the processing, interpretation, and integration with other data types. In this context, this study is the first use of T-LiDAR data to investigate quantitatively the speleothem morphology and distribution within a subterranean site—in this case, Golgotha Cave, SW Western Australia.

Most studies on karst systems show that variability in the infiltration processes governs both the location and the shape of stalactites [19], [26]–[27]. The karst literature describing the spatial distribution of speleothems mostly consists of qualitative descriptions [28]. Research on karstogenesis [19], [29] associates the presence of stalactites with typical growth factors, such as the presence of soils with high partial pressure of CO_2, water flow, and a low partial pressure of CO_2 in the cave atmosphere [30]. For example, [26] correlated the main speleothem shapes with different feed water regimes. However, such studies did not investigate the relationship between speleothem morphology and their location and relationship to karst structure. So far, only a few studies have quantitatively described speleothem spatial distributions in a cave system, or even in a chamber or passage of a cave [31].

According to [19], three levels of porosity can be distinguished within karst aquifers: 1) primary porosity associated with intergranular pores in the rock matrix; 2) secondary porosity associated with common rock discontinuities such as fractures (fissures) and bedding planes; and 3) tertiary porosity with solutionally enlarged voids such as channels and conduits developed from the initial discontinuities. Whereas groundwater flow in the matrix and small fissures is typically slow and laminar, flow in karst conduits (caves) is often fast and turbulent. Some hypothetical karst water flow pathways are illustrated schematically by [32] and [33], showing possible mechanisms by which water might be delivered to individual speleothems, although in reality combinations of these flow pathways will always occur. Thus, stalactite shape and water chemistry seem to be controlled by two water flow types in karstified limestone: 1) matrix flow, which is likely to homogenize the growth, shape, and chemistry of stalactites and 2) the fracture network that usually generates heterogeneities in secondary porosity causing variations in stalactite growth rate, shape, and chemistry.

We propose that the geometry of stalactites could indicate possible flow types or combinations of flow types. Stalactite morphology has long been studied. For example, [34] described the morphology of "soda-straw," the slender and hollow stalactites, and suggested some controlling factors in determining the smallest possible equilibrium diameter of a stalactite. Reference [35] modeled growth of solid stalactites as a free-boundary problem and compared the actual and theoretical stalactites shape. According to [36], soda-straw stalactites are the low discharge and low discharge variability end-member of speleothem that are associated with water ingress to a cave roof. On the other hand, at increasing discharge and discharge variability, typical forms are "icicle-shape stalactites" and "curtains." In these later morphologies, the stalactites thicken outward and downward with time, and often
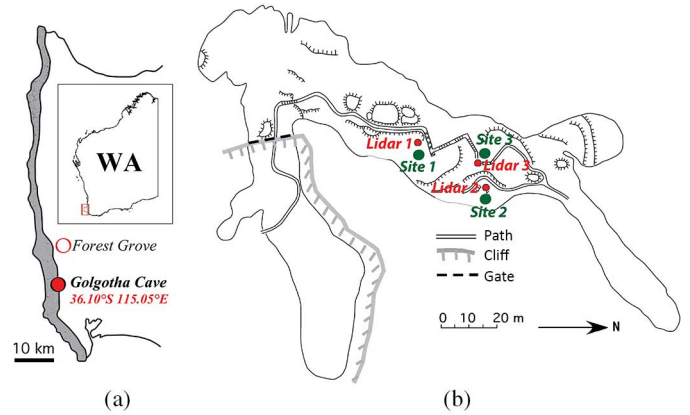

Fig. 1. (a) SW Western Australia map showing coastal belt of dune calcarenite (adapted from [38]) (inset indicates SW Western Australia region). (b) Plan view of Golgotha Cave map showing all three ceiling sites (green dots) and T-LiDAR positions (red dots).

a surface rippling is observed with a characteristics wavelength of approximately 1 cm.

The above literature suggests that hydrological flow properties could be identified from the geometry of stalactites and other morphological features in relation to the cave ceiling. In this study, we use T-LiDAR data to image a cave ceiling including individual stalactites. We, then, perform statistical and morphological analyses of cave ceiling comprising different sizes and shapes of stalactites. Among these, we analyze the spatial distribution of stalactites for various sites and establish relationships between stalactite diameter and length. We relate stalactite density variation with topographic elevation of the cave ceiling, indicating groundwater flow distribution governed by hydraulic gradient deviations. The role of the type of water flow processes (matrix or fracture flow) is also analyzed by studying the spatial distribution of a large population of stalactites in three sites within the same cave system.

II. SITE DESCRIPTION AND DATA ACQUISITION

SW Western Australia has a Mediterranean-type climate, with dry summers and wet winters associated with the seasonal migration of the midlatitude westerly winds. Rainfall, recorded at Forest Grove [34.07°S 115.10°E, weather station number: 9547; Fig. 1(a)] 5 km from our monitored site since 1926, is 1136.8 ± 184 mm annually with approximately 75% of the annual rainfall occurring between May and September [37]. Mean maximum daily temperatures range from 16 °C (61 F) in July to 27 °C (81 F) in February.

The field site, Golgotha Cave [36.10°S 115.05°E, Fig. 1(a)], is in aeolianites (dune limestone) of Quaternary age, which are wind-blown calcareous sands that have deposited widely around the coast of Australia. The cave is 200-m long and up to 25-m wide, and the dune limestone is 20–30-m thick over the cave [Fig. 1(b)]. Vadose zone water flow, and subsequent widening by ceiling collapse, formed the cave chamber.

The T-LiDAR measurements were taken adjacent to two locations where cave drip waters have been sampled for drip rate and chemistry for the previous 10 years (2005–2014) [38].

These two areas of the cave have contrasting discharge, dune facies, and karst features [38] that make these two sites more interesting in terms of water flow and are known as site 1 (located approximately 60 m into the cave) and site 2 (located a further 30 m into the cave). Site 3 is in-between sites 1 and 2 [Fig. 1(b)] where we also find significant drip water discharge and recent stalactite formations. Moreover, the T-LiDAR positions 1, 2, and 3 were selected such as to cover the significant portions of the ceiling from a perspective close to vertical to minimize the occlusion of other stalactites further away from the scanner line-of-sight. Another criterion for site selection was the accessibility of the site within the cave.

Site 1 ceiling contains straw stalactites that tend to cluster in the areas of lowest elevation. Sites 2 and 3 are in a large chamber, which appears to be less stable than that housing site 1, as evidenced by roof-collapse, dense rubble on the floors, and small breakdown chambers in the walls and ceilings [38]. Stalactites in site 2 tend to be more isolated, emerging either along fractures or at the margins of relict dune surfaces revealed by roof-collapse, indicating the possibility of lateral flow dispersion.

In this study, a FARO Focus3D terrestrial LiDAR has been used to acquire 3-D geological images of the cave ceiling of all three sites with detailed stalactite distribution from a single point in each site. The resulting point-cloud provides detailed omnidirectional information on the cave morphology and the stalactite size and shape. Each scan lasts approximately 10 min with a resolution of 1 mm. The point-cloud from all three sites are cropped to retain only significant portions of the ceiling that have a clear view of the stalactite distribution, and to efficiently manage the data storage requirements and reduce the computational time. Cropping is done using the SCENE 3-D laser scanner software, which was also used for 3-D visualization, meshing, and file formats conversion. After cropping, the point-clouds were exported to MATLAB for further processing.

For site 1 and with a coarsened resolution of 4 mm, the cropped data set comprises 1.9×10^6 measurements within a total ceiling area of 9.5 m × 3.2 m [Fig. 2(a)]. This portion of ceiling has two areas that consist of stalactites, the left portion having smaller ones [zone 1 in Fig. 2(b)] and the right side with longer ones [zone 2 in Fig. 2(b)]. Fig. 3(a) shows site 2, which has a lower ceiling elevation compared to the other sites. The cropped data set, we have used, for site 2 comprises 3.45×10^6 measurements with a resolution of 4 mm and a total ceiling area of 8 m × 6.9 m shown in Fig. 3(b). Site 3 is shown in Fig. 4 having a total of 1.406×10^6 measurement points with a ceiling area of 4.5 m × 5.0 m.

III. CEILING TOPOGRAPHY ANALYSIS

The stalactite shapes were analyzed using a two-stage procedure. In a first stage, we carry out a statistical analysis of the shape of all the stalactites measured, without taking into account their spatial distribution. The second stage involves a spatial study of the data set to examine possible correlations between stalactite shape and geographical location, and later develop a relationship with water flow distribution.
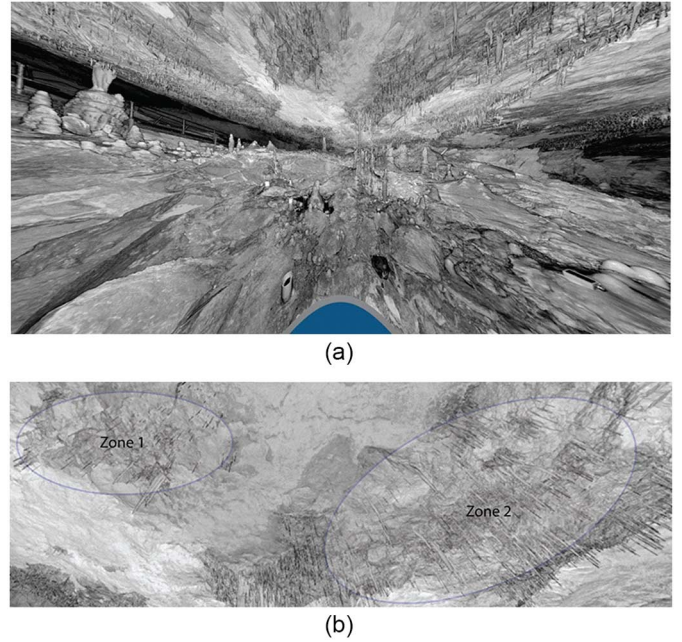

(a)

(b)

Fig. 2. (a) T-LiDAR scan of site 1. The blue half circle mark indicates the base of the T-LiDAR. (b) Site 1 ceiling portion considered for morphological analysis. Ellipses indicate the two zones in stalactites cluster.
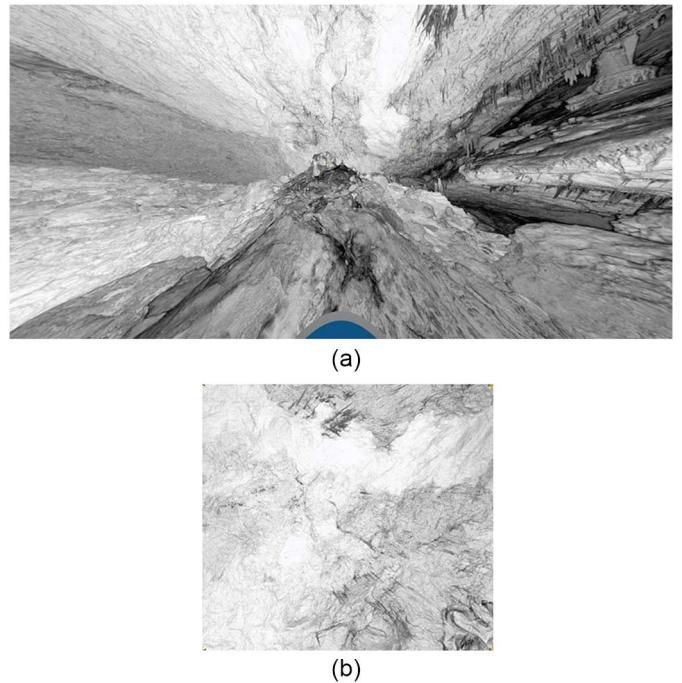

(a)

(b)

Fig. 3. (a) T-LiDAR scan of site 2. The blue half circle mark indicates the base of T-LiDAR. (b) Ceiling portion of site 2 considered for morphological analysis.

A. Identification of Stalactites

This section describes the methodology, we have used, to identify individual stalactites based on the T-LiDAR point-cloud. The original 1-mm data are interpolated to a resolution of 4 mm that is sufficient for the purpose of identifying individual stalactites, even soda-straw stalactites as [34] suggested the minimum diameter of soda-straw stalactite is 5.1 mm. Higher
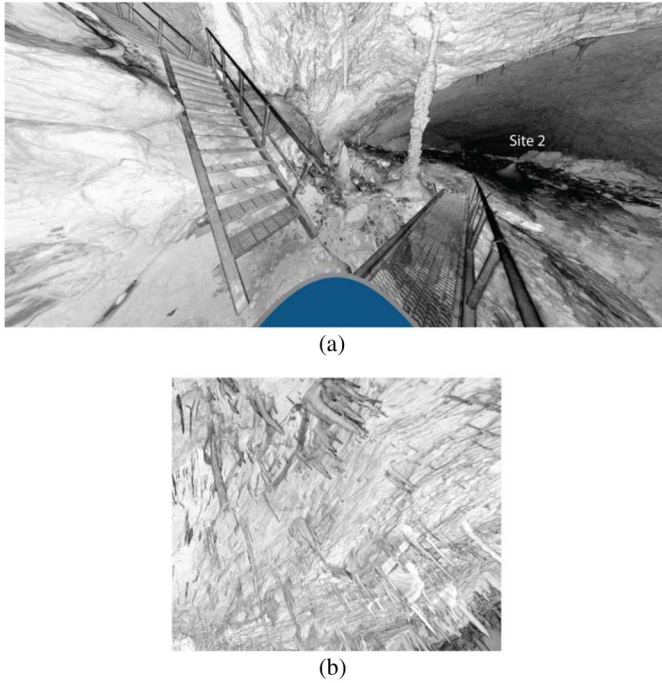
Fig. 4. (a) T-LiDAR scan of site 3. The blue half circle mark indicates the base of T-LiDAR. Site 2 is far in the right top corner of this image. (b) Ceiling portion of site 3 considered for morphological analysis.

resolution data would make it difficult to differentiate between small stalactites and natural rock surface variability. Moreover, the decreased resolution allows for smaller data set storage and faster processing time, which would be needed if applying our methodology to a full-scale case study. An initial processing step of the T-LiDAR data is to separate the ceiling surface into two components: 1) the general trend (low-frequency component corresponding to the overall ceiling topography) and 2) the small-scale fluctuations (high-frequency component corresponding to small dissolution and precipitation features, most notably stalactites), from where we can extract the stalactite information. This is accomplished by computing the moving-window average $M(x, y)$ of the surface [Fig. 5(b)], which results in a smooth surface representing the low-frequency component of the ceiling topography. Different possibilities for the size of the window for the moving average have been tested, including a variogram analysis where the variogram range gives the size of the structures on the surface considered. As a result, a window of 40×40 grid cells is found to be optimal for the separation of high-frequency and low-frequency fluctuations for all three sites. Then the high-frequency surface anomalies $A(x, y)$ are obtained by subtracting the moving average $M(x, y)$ [Fig. 5(b)] from original ceiling surface topography $T(x, y)$ shown in Fig. 5(a)

$$A(x, y) = M(x, y) - T(x, y). \qquad (1)$$

The anomaly surface $A(x, y)$ shown in Fig. 5(c) reflects the occurrence of stalactites. Locations of stalactites are found by isolating all pixels having an anomaly higher than a given threshold. This threshold is defined based on the histogram of $A(x, y)$ (Fig. 6). Our tests showed that for the sites investigated

in this study, a threshold defined as the 97th percentile of the topography anomalies allowed the appropriate identification of individual stalactites (vertical red lines shown in Fig. 6).

The thresholding operation results in a binary variable $B(x, y)$ that represents the occurrence of anomalies in the surface, believed to correspond to stalactites. While this binary variable indicates the presence or absence of a stalactite, it cannot be directly used to separate individual stalactites. The morphology of a stalactite on a cave ceiling can be conceptualized as an anomaly in the topography that is not connected to other anomalies. In this definition, it is assumed that each stalactite is a separate object, disconnected from the other stalactites. To apply this principle, we use a connected component analysis [39], [40], which is applied to $B(x, y)$ to distinguish individual stalactites. Each identified connected component then corresponds to a separate stalactite. Statistics can be computed on properties of the connected components such as their area or their shape. Across all three sites considered, this methodology allows automated identification of 5075 stalactites on a total area of almost 108 m^2.

$B(x, y)$ depends on the threshold value and to a lesser extent on the size of the window used for computing the moving average. In particular, a lower threshold will result in stalactites located close to each other being grouped in a single large connected component. Increasing or decreasing this threshold changes the size of all connected components, in the same way as a changing water level emerges or submerges islands. Similarly, different threshold values can be used to reveal different morphological properties of the stalactite clusters. Thus, our analysis uses two possible threshold values: 1) the 97th percentile of the topography anomalies is used to identify individual stalactites and 2) the 94th percentile is used to identify stalactites clusters (vertical red and green lines shown in Fig. 6).

The segmentation process is semiautomated, in the sense, that the user controls parameters (i.e., moving average window size, threshold), which are specific to a particular cave site. It is known [41] that such parameterization necessarily involves a tradeoff balance between over- and undersegmentation. In other terms, one may either mistake a single stalactite cluster for multiple nearby stalactites, or, on the other hand, merge several individual stalactites into a single cluster. While the optimal parameters minimize both types of error, there is generally no parameters combination that results in a perfect, error-free segmentation. Here, identifying stalactites clusters using a 94th percentile threshold is highly a sensitive parameter, because incorrectly classified clusters often represent the most extreme outliers in the segmented flow types and can, therefore, substantially affect the flow classification.

B. Stalactite Morphology

The identification of separate stalactites on the cave ceiling, together with the detailed topography information, allows computing the length and diameter of each stalactite. Fig. 7(a) shows the relationship between stalactite length and diameter excluding soda-straw stalactites, which are characteristically nonplatonic and have a variable length and a typical width of
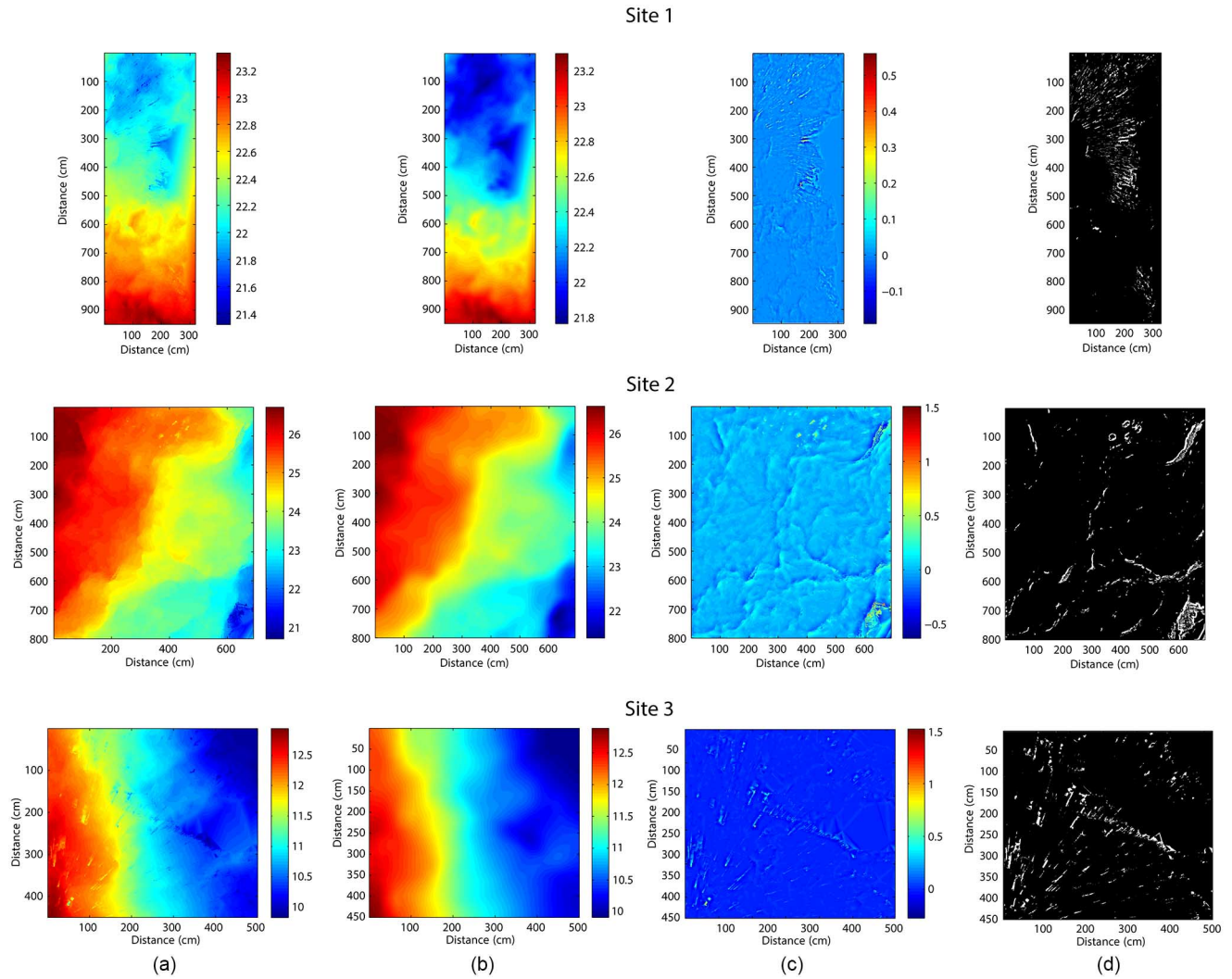
Fig. 5. (a) Cave ceiling topography in 2-D $T(x, y)$. (b) Moving averages with a window of 40 grid pixels $M(x, y)$. Color scales represent elevations in meters relative to the T-LiDAR receiver. (c) Topographic anomalies maps $A(x, y)$. (d) Locations of stalactites $B(x, y)$ representing pixels where topography anomalies are above the threshold.
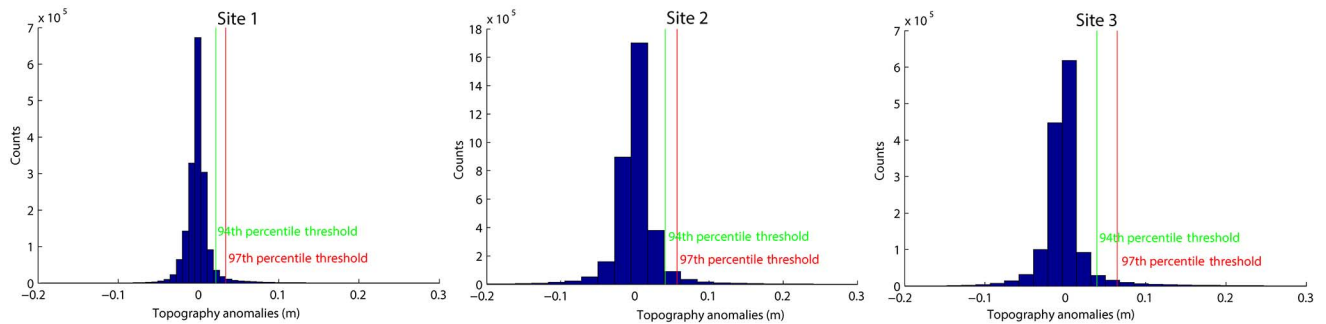

Fig. 6. Histograms of the topography anomalies and threshold used to identify the individual stalactites (97th and 94th percentile thresholds, shown as vertical red and green lines).

about 5–10 mm. Fig. 7(b) displays the relationship between stalactite length and ceiling elevation relative to the T-LiDAR receiver. We have used a separate coordinate system for each site, using the LiDAR position as origin. This is appropriate for our purpose since we are only interested in characterizing the morphological properties of each site. Hence, in Fig. 7(b), the Z coordinate of the ceiling position represents, for each site,

the elevation above the T-LiDAR. In this context, ceiling elevation is an indicator of the column of water pressure over a given volume of rock (vertical hydraulic gradient) and is investigated here as a possible driver for the occurrence of stalactites within a particular site.

Due to the large number of points in the plots of Fig. 7, we chose to display these relationships as density estimates by the
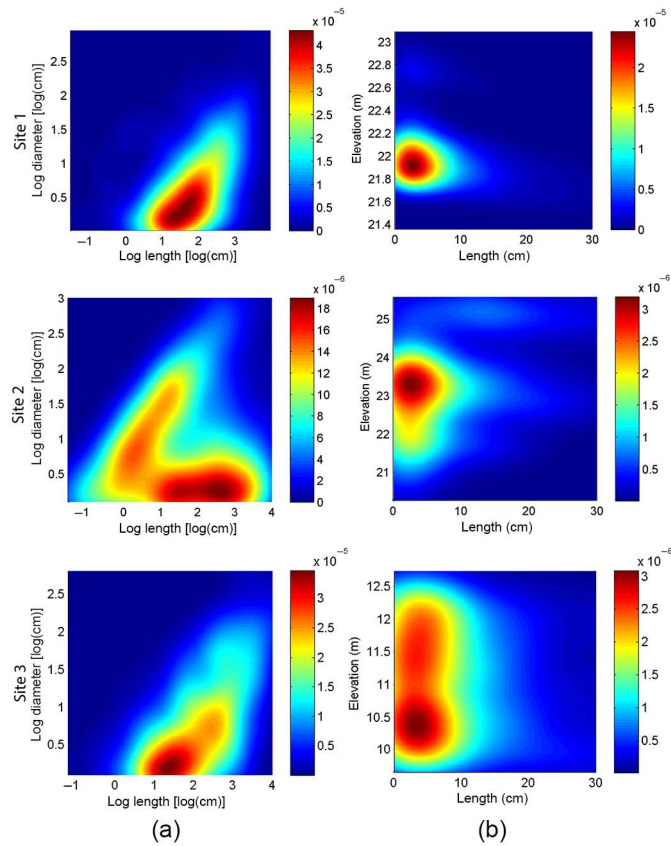
Fig. 7. Scatterplots with application of kernel smoothing. (a) Stalactite length versus diameter excluding soda-straw stalactites. (b) Stalactite length versus ceiling elevation plots. The elevations are relative to the T-LiDAR position. Color scales represent probability. Lengths and diameters are in cm and the x-axis scales are all different.

Fig. 8. Identification of flow type based on aspect ratio of stalactite-connected components. The ceiling portion is taken from site 2.

application of kernel smoothing [42]. The reason for applying kernel smoothing is that most data points are superimposed in the scatter plot and it is, therefore, difficult to visualize the density of points. Kernel smoothing constructs a small Gaussian shape (called kernel) on top of each point, then sums all of these kernels. It allows more accurate display of the density of points that are, otherwise, not visible in a scatter plot.

C. Determination of Flow Type

We differentiate different types of flow patterns using two properties of the stalactites: 1) aspect ratio and 2) cross-sectional area. The aspect ratio denotes the ratio of the major axis to the minor axis in the ceiling surface of an individual connected component (an individual stalactite or a cluster of stalactites). Cross-sectional area is the area of the stalactite section in the ceiling surface. Based on the typical types of porosity and infiltration processes in karst, we define three categories of flow and identify their spatial signature according to the following criteria.

1) Type 1: Matrix flow that is caused by water seeping through the rock matrix. It includes smaller fractures, typically creating icicle-shape stalactites and defined by lower aspect ratio, and lower cross-sectional area of individual stalactites. Within this definition, we differentiate
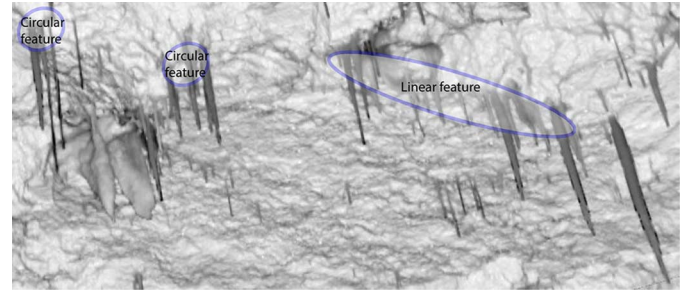
soda-straw stalactites that are further characterized by lower stalactites diameter and a higher length/diameter ratio. Soda-straw stalactites are an important feature of matrix flow and do not follow the platonic ideal shape. Groundwater flow processes through the porous limestone matrix are essentially the same as groundwater flow in porous media [46], and can be described using the matrix flow formulation of Darcy, which states that the discharge is proportional to the hydraulic gradient and the cross-sectional area, with the hydraulic conductivity being the proportionality factor [44].

2) Type 2: Pure fracture flow where water circulates within the fractures openings. It typically forms curtain-shape stalactites or groups of stalactites aligned in the direction of highest fracturing (such as the linear feature shown in Fig. 8) and defined by a higher aspect ratio of stalactite clusters. The fracture flow formulation simplifies the fractures to have parallel walls and uniform aperture [45]. Assuming impermeability for fracture walls, the steady-state flow rate can be described by the cubic law derived from Navier–Stokes equation for a viscous and incompressible fluid [44].

3) Type 3: Combination of conduit, fracture, and matrix flow, which typically forms circular features as shown in Fig. 8 and defined by lower aspect ratios of stalactite cluster and a higher cross-sectional area of stalactites. Combination of different processes can occur, e.g., when conduits are the result of preferential calcite dissolution along preexisting fractures, or if the base of the pipe conduit is closed, resulting in a stalactite cluster. The resulting conduit networks are the key phenomenon that separates karst aquifers from porous and fractured-rock aquifers. Corresponding karst aquifers include conduits with both rapid flow with low storativity and no flow with high storativity. The flow in conduits can occur as a free surface open-channel regime driven by gravitational gradients, as a pipe flow under pressure, with the possibility of both occurring in different reaches of a conduit. Alternatively, the conduit could have no flow, providing a water store [44].

The detailed classification criteria is summarized in Fig. 9 and the overall rationale can be described as follows. Since flow type 1 is related to discrete features of very limited spatial extent (fractures and conduits), we define the locations of flow type 1 according to the geometry of individual
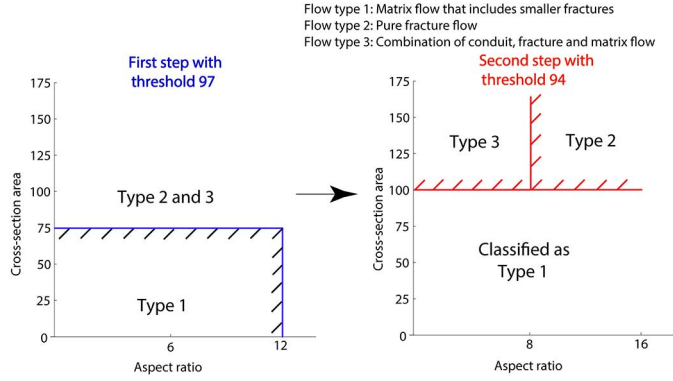
Fig. 9. Flow type classification criteria based on aspect ratio and cross-sectional area.

stalactites. These are identified based on a threshold at the 97th percentile of $A(x,y)$. Using this threshold, locations with cross-sectional area $<75\,\mathrm{cm}^2$ and connected component aspect ratio <10 are defined as flow type 1, including the soda-straw stalactites, which we further define by diameter $<10\,\mathrm{mm}$ with a length/diameter ratio >8.

To validate our approach, we manually counted both icicle-shape and soda-straw stalactites visible in the high-resolution T-LiDAR image and compared that to those features classified from the morphological analysis. As it is difficult to manually classify large portions of the ceiling, a smaller ceiling portion was taken from site 2, and the optimum parameters were selected through this validation process (Fig. 10). The chosen parameters were then used for analysis of the larger images in later analyses. The individual stalactites in both high-resolution T-LiDAR image [Fig. 10(a)] and morphological analysis outcome [Fig. 10(b)] are presented. Table I compares the total number of stalactites identified using visual count and our automated methodology, for each stalactite type. Most icicle-shape stalactites are correctly identified. However, several soda straws close together could be misidentified as an icicle-shape stalactite, or a ceiling bedrock shape could be incorrectly classified as an icicle-shape stalactite. Another possibility might be the occlusion of sheltered soda-straw stalactites that are further away from the scanner line-of-sight and behind another large one from the angle where we took our LiDAR scans. Therefore, the number of soda-straw stalactites tends to be further underestimated.

We characterize flow types 2 and 3 based on a lower threshold that corresponds to the 94th percentile of $A(x,y)$. With this lower threshold, stalactites that are close to each other become grouped and form one large cluster. If a cluster has a large aspect ratio, it means that these stalactites have formed along a linear feature like a fracture or a fault (type 2), such as illustrated on the right side of Fig. 8. On the other hand, if this large cluster has a smaller aspect ratio, it means that this cluster of stalactites has a more circular shape, indicating a combination of conduit, fracture, and matrix flow (type 3), as on the left side of Fig. 8.

It should be noted here that using different threshold values for characterizing flow type 1 and flow types 2/3 causes the cross-sectional area of a connected component to change.

Hence, the areas defined as flow type 1, which have cross-sectional areas below $75\,\mathrm{cm}^2$, now have larger cross-sectional areas with the reduced threshold. We observed that the change in threshold resulted in a one-third increase of the area of the connected components, resulting in type 1 connected components having areas up to $100\,\mathrm{cm}^2$. In consequence, the areas of flow types 2 and 3 are defined as connected components with an area $>100\,\mathrm{cm}^2$ with a 94th percentile threshold (Fig. 9).

Among these larger clusters, the ones with a high aspect ratio (>8) are classified as pure fracture flow (type 2). The more circular ones (aspect ratio <8) are classified as type 3.

IV. RESULTS

A. Morphological Analysis of the Stalactites

Table II indicates the different threshold values used for each of the three sites considered, i.e., corresponding to 97th and 94th quantiles of $A(x,y)$. Based on these threshold values, we compute various cave ceiling statistical properties that are also presented in Table II, such as the number of stalactites and their densities, the range of values for stalactites diameter, the aspect ratios of connected components. The minimum stalactite diameter we found with 4-mm resolution is 0.51 cm for all sites, supporting the statement of [34]. The average length of the stalactites is larger for sites 2 and 3 compared to site 1, and on the other hand, the average aspect ratio of individual stalactites is larger for site 1.

We find moderate to low correlation coefficients (r) between stalactite diameters and lengths (0.62, 0.23, and 0.69 for sites 1, 2, and 3, respectively). The shape of these relationships [Fig. 7(a)] agrees with the platonic ideal of stalactite shape described by [35]. Numerical studies involving the simulation of stalactite growth and surface dynamics performed by [35] showed the existence of an attractor in the space of shapes, toward which stalactites will be drawn regardless of initial conditions. This ideal shape is scale-independent and is named the platonic ideal stalactite shape. It is described by a universal, parameter-free differential equation. The shape of any single real stalactite will vary from this ideal shape in a variety of ways due to instabilities such as those producing crenulations, inhomogeneous cave conditions, and unidirectional airflow. Mindful of this, [35] found that an average of natural stalactites appropriately cancels out these imperfections, and compares extremely well with the platonic ideal, which is the case of Fig. 7(a). The median gradients or ratio of diameter to length for all three sites are 1.10, 0.96, and 1.22, respectively, with interquartile ranges of 0.83, 1.4, and 1.12. The ratio of diameter to length for the platonic ideal stalactite found by [35] is 1.3. Our ratios are similar to lower, which is due to the presence of soda-straw stalactites shown in Table II and Fig. 11. All three sites have significant presence of soda-straw stalactites, which do not agree with the ideal stalactite shape [35] as they have low diameter to length ratios. Therefore, we perform the same test excluding the soda-straw stalactites and find the median gradients for all three sites 1.21, 1.35, and 1.32, respectively, with high interquartile ranges of 0.83, 1.8, and
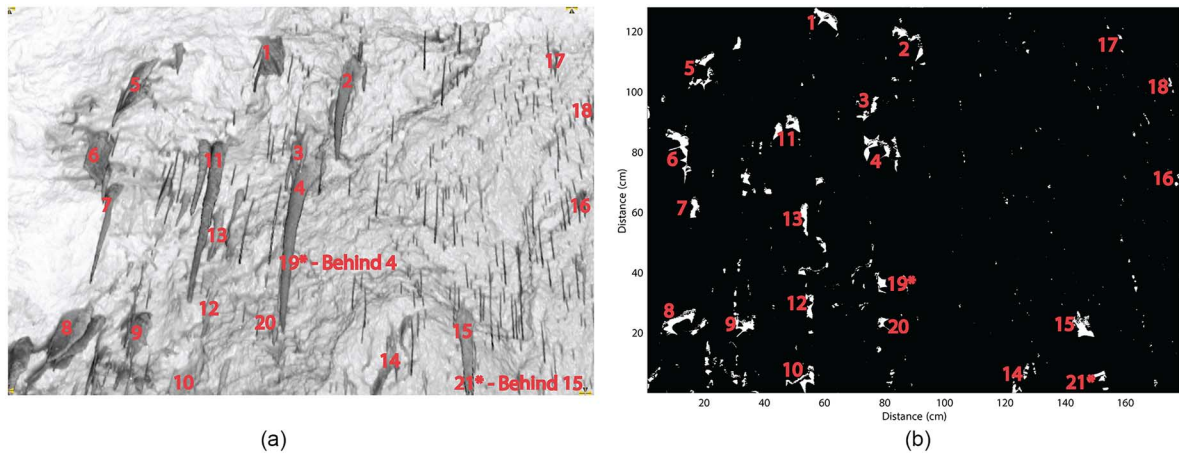
Fig. 10. (a) High-resolution T-LiDAR image of site 2 ceiling portion (125 cm × 175 cm) for validation process. Some stalactites are not visible in the T-LiDAR image (such as 19 and 21) from this angle due to the shadow of another stalactite, however, can be seen from an opposite view. (b) Locations of individual stalactite identified using the morphological analysis. Few stalactite locations are numbered to compare both the cases in terms of stalactite identification.

TABLE I
STALACTITE COUNT VALIDATION

Type of stalactites	Stalactite count	
	From actual T-Lidar image (visual count)	From morphological analysis
Icicle shape	≈ 60	62
Soda straw	≈ 100	81
Total	≈ 160	143

TABLE II
STALACTITE PROPERTIES FROM T-LiDAR DATA ANALYSIS

Stalactite properties	Site 1	Site 2	Site 3
Ceiling dimension	9.5 m × 3.2 m	8.0 m × 6.9 m	4.5 m × 5.0 m
Threshold corresponding to 97th quantiles of $A(x,y)$ (m)	0.0345	0.0577	0.0652
Threshold corresponding to 94th quantiles of $A(x,y)$ (m)	0.0188	0.0367	0.0324
Total number of stalactites	1909	2023	1143
Density of stalactites per m^2	68	37	51
Maximum diameter of one stalactite (cm)	19.2	51.6	16.6
Minimum diameter of one stalactite (cm)	0.51	0.51	0.51
Average length of stalactites (cm)	6.02	8.46	9.28
Maximum aspect ratio of individual stalactites	43.3	30.0	34.7
Minimum aspect ratio of individual stalactites	1.0	1.0	1.0
Average aspect ratio of individual stalactites	7.8	6.1	6.8
Correlation coefficient (r) between stalactite diameters and lengths	0.62	0.23	0.69
Gradients or ratio of stalactite diameters to lengths	1.21	1.35	1.32
Proportion of flow type 1 (% of the ceiling area with stalactites)	53.43	10.27	46.9
Proportion of flow type 2 (% of the ceiling area with stalactites)	37.84	56.01	24.46
Proportion of flow type 3 (% of the ceiling area with stalactites)	7.76	32.86	27.49
Proportion of soda straw stalactites (% of the ceiling area with stalactites)	0.97	0.86	1.14
Proportion of no flow area (% of total ceiling area)	96.54	91.79	97.21

1.05. These outcomes satisfy the platonic ideal stalactite shape, however, the high interquartile ranges represent a significant level of heterogeneity between the sites. From Fig. 7(b), the concentric pattern indicates that longer stalactites tend to occur in comparatively lower ceiling elevation, which we hypothesize represents greater hydraulic gradients within a ceiling area, i.e., greater mass of water in the limestone above the roof of the cave. This is evident for site 1, which is dominated by flow type 1 in the limestone roof, however, not that strongly apparent in sites 2 and 3 (Table II). The reason might be that the limestone porosity in these sites does not favor hydraulic gradients similar to site 1 due to the domination of fracture flow (as shown in Fig. 11). Also the cropped ceiling portion we consider for morphological analysis of site 1 consists of two nearby stalactite zones [Fig. 2(b)]. Among these two areas, the lower zone [with ceiling elevation less than 22.2 m in Fig. 5(a)] has longer stalactites representing the lower ceiling elevation, probably due to higher hydraulic gradient at low elevation.

B. Flow Pattern

The locations of various flow types for different sites are shown in Fig. 11. For each site, we compute the proportions of the ceiling representing different flow types and also no flow area (Table II). We find significant counts of soda-straw stalactites in all three sites that also fall within flow type 1, however, the proportions are little, approximately 1% of the ceiling area with stalactites (Table II). From the flow patterns illustrated in Fig. 11 and the proportions provided in Table II, it is apparent that both sites 1 and 3 are mostly dominated by flow type 1: matrix flow representing water flowing down and seeping through rock matrix. The wide distributions of both icicle-shape and soda-straw stalactites in these two sites reflect seepage flow to cave roof from overlying late Quaternary Aeolian sandstone aquifer. In this case, water movement will
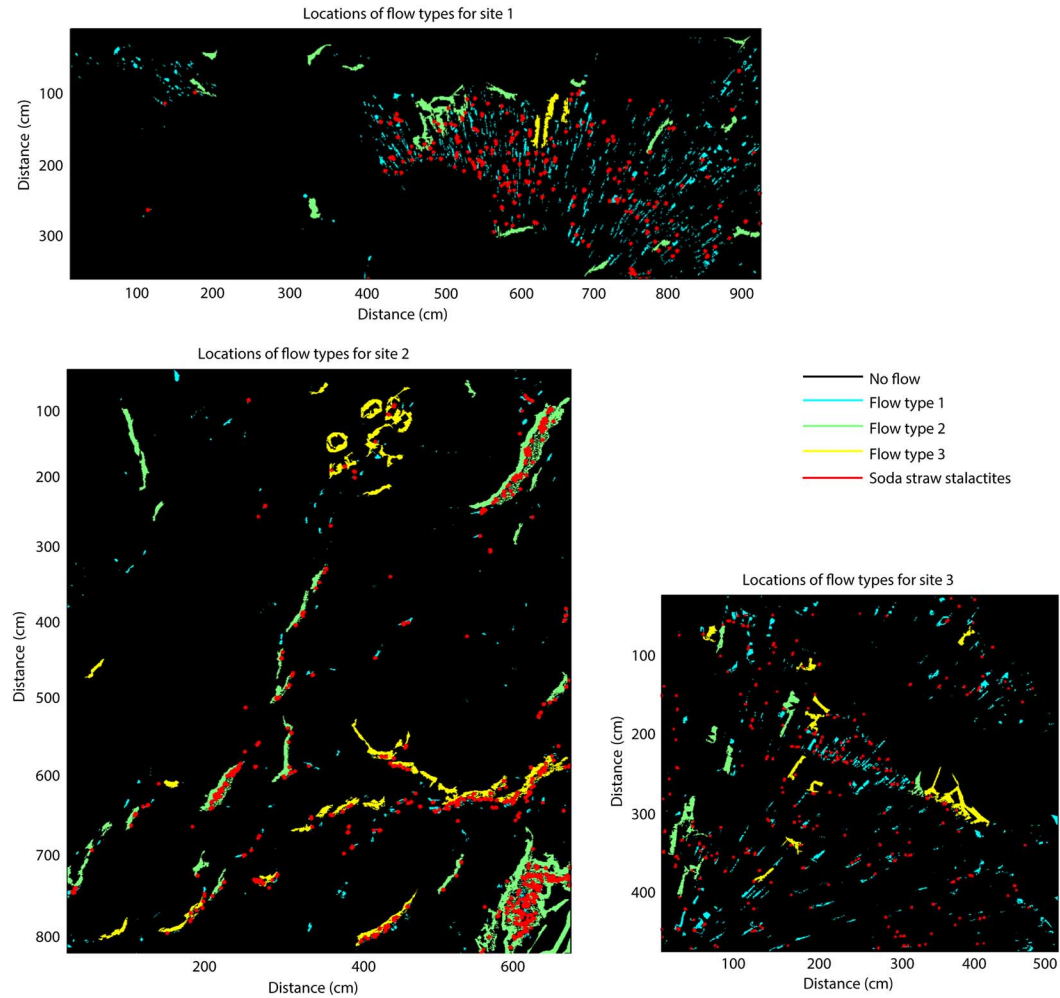
Fig. 11. Flow patterns at different sites. The center of red dots represents the location of soda-straw stalactites. We emphasize the locations by increasing five times the size of the dots.
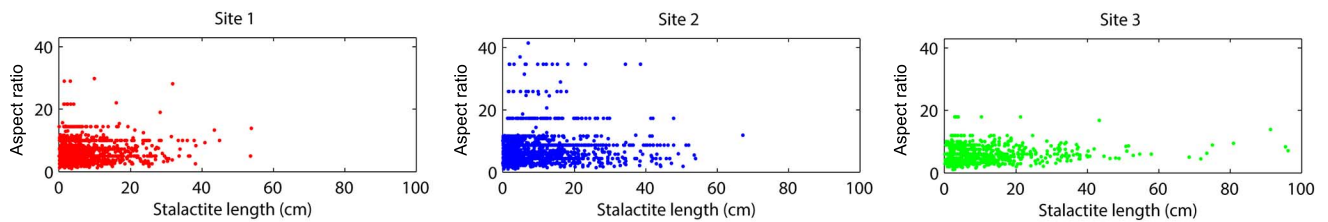

Fig. 12. Aspect ratio versus length of stalactite clusters for all three sites.

be a function of the primary porosity of the karst, with flow rates proportional to the matrix permeability. In such cases of dominant flow type 1, rates of change of water movement are likely to be slow, with slow drip rates of low variability [36]. Based on the size and shape of stalactite clusters, we find site 2 typically controlled by flow type 2 (Fig. 11). Therefore, this site is dominated by water flowing down through a fracture. In this site, drip rates are likely to vary over time, depending upon the mode of water delivery to the preferential flow system. The latter will reflect the surface water balance, including evapotranspiration rates and precipitation, in addition to potential water storage within the epikarst [43].

C. Aspect Ratio and Stalactite Length

Fig. 12 shows the relationship between the aspect ratio of stalactite clusters and the average length of individual stalactites in a given cluster for all three sites. The aspect ratio represents the anisotropy in the shape of stalactite clusters, with larger values for linear features. We observe that the more compact clusters of stalactites having lower aspect ratios are made of longer stalactites, indicating more continuous flow in case of both sites 2 and 3. The average lengths of stalactites are slightly larger for both these sites compared to site 1 (Table II). The analysis demonstrates a spatial variability, with more linear groups of stalactites present in site 2 compared to sites

1 and 3, which supports the dominant proportions of fracture flow described in Table II. We hypothesize that there are solution features above the cave roof, which provide the necessary dissolution of limestone and then storage of super-saturated water.

V. Conclusion

Caves make it possible to enter an aquifer formation to directly capture 3-D point-clouds and study a subsurface karst system that would be otherwise inaccessible. We present the first quantitative analysis of the morphology and spatial distribution of stalactites covering a cave ceiling surface. By performing statistical and morphological analysis of karstic features based on T-LiDAR data, we have been able to identify flow processes through saturated conduits, fractures, and the matrix, and how these are expressed in the geological structures.

The relationships between stalactite diameter and length are established that are in agreement with the expected typical stalactite shape. A significant correlation between the length of the stalactites and the topographic elevation of the cave ceiling indicates that higher hydraulic gradient favors groundwater movement through karstified limestone.

Three nearby sites in the same cave exhibit very different behaviors, which give insights into the degree of heterogeneity of the flow types. This dynamic variation in karst processes has important implications for speleothem research since it can help explaining the differences in paleoclimate record from nearby speleothems [36], [47].

An avenue for future research is to map the extent of cave damage (e.g., by touristic exploitation or in speleoseismology) using the deviations from the ideal model shape of [35], with broken stalactites having a shorter length to diameter ratio. Assessment and environmental management of tourist caves might then be possible using recurrent surveys from the same location. Repetitive T-LiDAR measurements could also be used to measure speleothem growth rates in environments where this growth is extremely fast, such as in caves where speleothems form from lime (reaction $CaO + CO_2 = CaCO_3$) and having growth rates of about 1 cm/year [48], [49]. Another possible application of T-LiDAR data, in the field of speleoseismology, is to look at deviations of stalactite shapes from a linear length-distance trend and any relationship to the extent of fracturing that assists to work out the earthquake history.

VI. Avenue for Future Research

In future research, we plan to use stalactite distribution derived from T-LiDAR data to create training images for the generation of large synthetic cave systems and conduct virtual tracing experiments in formations that cannot be explored in detail.

Acknowledgment

References

[1] S. C. Charleston, *LiDAR 101: An Introduction to LiDAR Technology, Data, and Applications*. Charleston, SC, USA: National Oceanic and Atmospheric Administration (NOAA) Coastal Services Center, Nov. 2012.

[2] P. Passalacqua, J. Hillier, and P. Tarolli, "Innovative analysis and use of high-resolution DTMs for quantitative interrogation of Earth-surface processes," *Earth Surf. Processes Landforms*, vol. 39, no. 10, pp. 1400–1403, 2014.

[3] P. A. Zandbergen, "Characterizing the error distribution of LiDAR elevation data for North Carolina," *Int. J. Remote Sens.*, vol. 32, no. 2, pp. 409–430, 2011.

[4] Q. Zeng, X. Xie, Y. Zhang, Y. Ye, Y. Hu, and S. Liu, "Digital outcrop modeling and geology information extraction based on ground-based Lidar," presented at the Int. Conf. Audio, Language and Image Processing (ICALIP), Jul. 16–18, 2012, pp. 580–583.

[5] J. C. Fernandez-Diaz *et al.*, "Early results of simultaneous terrain and shallow water bathymetry mapping using a single-wavelength airborne LiDAR sensor," *IEEE J. Sel. Topics Appl. Earth Observ. Remote Sens.*, vol. 7, no. 2, pp. 623–635, Feb. 2014.

[6] D. G. Milledge, S. N. Lane, and J. Warburton, "The potential of digital filtering of generic topographic data for geomorphological research," *Earth Surf. Processes Landforms*, vol. 34, no. 1, pp. 63–74, 2009.

[7] J. Sauber, M. Hofton, R. Bruhn, S. Luthcke, and B. Blair, "DESDynI LiDAR for solid earth applications," presented at the IEEE Int. Geoscience and Remote Sensing Symposium (IGARSS), Jul. 25–30, 2010, pp. 1903–1906.

[8] C. Babcock, J. Matney, A. O. Finley, A. Weiskittel, and B. D. Cook, "Multivariate spatial regression models for predicting individual tree structure variables using LiDAR data," *IEEE J. Sel. Topics Appl. Earth Observ. Remote Sens.*, vol. 6, no. 1, pp. 6–14, Feb. 2013.

[9] S. Guoqing and K. J. Ranson, "Modeling LiDAR returns from forest canopies," *IEEE Trans. Geosci. Remote Sens.*, vol. 38, no. 6, pp. 2617–2626, Nov. 2000.

[10] W. Ni-Meister, D. L. B. Jupp, and R. Dubayah, "Modeling LiDAR waveforms in heterogeneous and discrete canopies," *IEEE Trans. Geosci. Remote Sens.*, vol. 39, no. 9, pp. 1943–1958, Sep. 2001.

[11] J. Vauhkonen *et al.*, "Classification of spruce and pine trees using active hyperspectral LiDAR," *IEEE Geosci. Remote Sens. Lett.*, vol. 10, no. 5, pp. 1138–1141, Sep. 2013.

[12] A. P. H. L. Cracknell, *Introduction to Remote Sensing*. New York, NY, USA: Taylor & Francis, 2006.

[13] D. Nedeljkovic, A. Hauchecorne, and M. L. Chanin, "Rotational Raman LiDAR to measure the atmospheric temperature from the ground to 30 km," *IEEE Trans. Geosci. Remote Sens.*, vol. 31, no. 1, pp. 90–101, Jan. 1993.

[14] M. Sicard *et al.*, "Aerosol LiDAR intercomparison in the framework of SPALINET—The Spanish LiDAR network: Methodology and results," *IEEE Trans. Geosci. Remote Sens.*, vol. 47, no. 10, pp. 3547–3559, Oct. 2009.

[15] A. Casas, S. N. Lane, D. Yu, and G. Benito, "A method for parameterising roughness and topographic sub-grid scale effects in hydraulic modelling from LiDAR data," *Hydrol. Earth Syst. Sci.*, vol. 14, pp. 1567–1579, 2010.

[16] Y. Wei and U. Stilla, "Comparison of two methods for vehicle extraction from airborne LiDAR data toward motion analysis," *IEEE Geosci. Remote Sens. Lett.*, vol. 8, no. 4, pp. 607–611, Jul. 2011.

[17] S. Peeri, J. V. Gardner, L. G. Ward, and J. R. Morrison, "The seafloor: A key factor in LiDAR bottom detection," *IEEE Trans. Geosci. Remote Sens.*, vol. 49, no. 3, pp. 1150–1157, Mar. 2011.

[18] S. Tang, P. Dong, and B. P. Buckles, "A new method for extracting trees and buildings from sparse LiDAR data in urban areas," *Remote Sens. Lett.*, vol. 3, no. 3, pp. 211–219, 2011.

[19] D. Ford and P. D. Williams, *Karst Hydrogeology and Geomorphology*. Hoboken, NJ, USA: Wiley, 2007.

[20] M. Hammerle, B. Hofle, J. Fuchs, A. Schroder-Ritzrau, N. Vollweiler, and N. Frank, "Comparison of kinect and terrestrial LiDAR capturing natural karst Cave 3-D objects," *IEEE Geosci. Remote Sens. Lett.*, vol. 11, no. 11, pp. 1896–1900, Nov. 2014.

[21] J. Bellian, C. Kerans, and D. Jennette, "Digital outcrop models: Applications of terrestrial scanning LiDAR technology in stratigraphic modeling," *J. Sediment. Res.*, vol. 75, no. 2, pp. 166–176, 2005.

[22] I. Fabuel-Perez, D. Hodgetts, and J. Redfern, "A new approach for outcrop characterization and geostatistical analysis of a low-sinuosity fluvial-dominated succession using digital outcrop models: Upper Triassic Oukaimeden Sandstone Formation, central High Atlas, Morocco," *AAPG Bull.*, vol. 93, pp. 795–827, 2009.

[23] J. K. Pringle, J. A. Howell, D. Hodgetts, A. R. Westerman, and D. M. Hodgson, "Virtual outcrop models of petroleum reservoir analogues: A review of the current state-of-the-art," *First Break*, vol. 24, pp. 33–42, 2006.

[24] A. Rotevatn, S. J. Buckley, J. A. Howell, and H. Fossen, "Overlapping faults and their effect on fluid flow in different reservoir types: A LiDAR-based outcrop modeling and flow simulation study," *AAPG Bull.*, vol. 93, pp. 407–427, 2009.

[25] P. Wilson, D. Hodgetts, F. Rarity, R. L. Gawthorpe, and I. R. Sharp, "Structural geology and 4D evolution of a half-graben: New digital outcrop modelling techniques applied to the Nukhul half-graben, Suez rift, Egypt," *J. Struct. Geol.*, vol. 31, no. 3, pp. 328–345, 2009.

[26] C. A. Hill and P. Forti, *Cave Minerals of the World*. Huntsville, AL, USA: National Speleological Society, 1997.

[27] A. B. Klimchouk, D. C. Ford, A. N. Palmer, and W. Dreybrodt, *Speleogenesis and Evolution of Karst Aquifers*. Huntsville, AL, USA: National Speleological Society, 2000.

[28] C. N. Jex *et al.*, "Spatially dense drip hydrological monitoring and infiltration behaviour at the Wellington Caves, South East Australia," *Int. J. Speleol.*, vol. 41, no. 2, pp. 283–296, 2012.

[29] R. Maire, "La haute montagne calcaire (karsts, cavités, remplissages, Quaternaire, paléoclimats)," *Karstologia Mémoire*, no. 3, 731 p., 1990.

[30] F. Bourges, P. Genthon, A. Mangin, and D. D'Hulst, "Microclimates of l'aven d'Orgnac and other french limestone caves (Chauvet, Esparros, Marsoulas)," *Int. J. Climatol.*, vol. 26, no. 12, pp. 1651–1670, 2006.

[31] Y. Perrette and J. Stéphane, "Spatial distribution of soda straws growth rates of the Coufin Cave (Vercors, France)," *Int. J. Speleol.*, vol. 39, pp. 61–70, 2010.

[32] C. Bradley, A. Baker, C. N. Jex, and M. J. Leng, "Hydrological uncertainties in the modelling of cave drip-water δ18O and the implications for stalagmite palaeoclimate reconstructions," *Quat. Sci. Rev.*, vol. 29, no. 17–18, pp. 2201–2214, 2010.

[33] A. Baker and I. J. Fairchild, "Drip water hydrology and speleothems," *Nat. Educ. Knowl.*, vol. 3, no. 10, p. 16, 2012.

[34] L. R. Curl, "Minimum diameter stalactites," *Bull. Nat. Speleol. Soc.*, vol. 34, pp. 129–136, 1972.

[35] M. B. Short, J. C. Baygents, J. W. Beck, D. A. Stone, R. S. Toomey, and R. E. Goldstein, "Stalactite growth as a free-boundary problem: A geometric law and its platonic ideal," *Phys. Rev. Lett.*, vol. 94, no. 1, p. 018501, 2005.

[36] I. J. Fairchild and A. Baker, *Speleothem Science: From Process to Past Environments*. Hoboken, NJ, USA: Wiley-Blackwell, 2012, 450 pp.

[37] Bureau of Meteorology. (2014). *Climate Statistics (Station 9547)* [Online]. Available: http://www.bom.gov.au/climate/data/, accessed on Dec. 20, 2014.

[38] P. C. Treble *et al.*, "An isotopic and modelling study of flow paths and storage in quaternary calcarenite, SW Australia: Implications for speleothem paleoclimate records," *Quat. Sci. Rev.*, vol. 64, pp. 90–103, 2013.

[39] P. Renard and D. Allard, "Connectivity metrics for subsurface flow and transport," *Adv. Water Resour.*, vol. 51, pp. 168–196, 2013.

[40] J. Serra and P. Soille, *Mathematical Morphology and Its Applications to Image Processing*. Norwell, MA, USA: Kluwer, 1994.

[41] J. Hyyppa, O. Kelle, M. Lehikoinen, and M. Inkinen, "A segmentation-based method to retrieve stem volume estimates from 3-D tree height models produced by laser scanners," *IEEE Trans. Geosci. Remote Sens.*, vol. 39, no. 5, pp. 969–975, May 2001.

[42] B. W. Silverman, *Density Estimation for Statistics and Data Analysis*. Boca Raton, FL, USA: CRC Press, 1986.

[43] J. W. Delleur, *The Handbook of Groundwater Engineering*, 2nd ed. Boca Raton, FL, USA: CRC Press, 2006.

[44] R. Ghasemizadeh *et al.*, "Review: Groundwater flow and transport modeling of karst aquifers, with particular reference to the North Coast Limestone aquifer system of Puerto Rico," *Hydrogeol. J.*, vol. 20, no. 8, 1441–1461, 2012.

[45] W. B. White and E. L. White, "Ground water flux distribution between matrix, fractures, and conduits: Constraints on modeling," *Speleogenesis Evol. Karst Aquifers*, vol. 3, pp. 1–6, 2005.

[46] P. W. Williams, "The role of the epikarst in karst and cave hydrogeology: A review," *Int. J. Speleol.*, vol. 37, no. 1, pp. 1–10, 2008.

[47] G. Mariethoz, B. F. J. Kelly, and A. Baker, "Quantifying the value of laminated stalagmites for paleoclimate reconstructions," *Geophys. Res. Lett.*, vol. 39, no. 5, 2012, doi: 10.1029/2012GL050986, Article ID: L05407.

[48] A. Baker, C. J. Proctor, and W. L. Barnes, "Variations in stalagmite luminescence laminae structure at Poole's Cavern, England, AD 1910±1996: Calibration of a palaeoprecipitation proxy," *Holocene*, vol. 9, no. 6, pp. 683–688, 1999.

[49] H. S. Sundqvist, A. Baker, and K. Holmgren, "Luminescence variations in fast-growing stalagmites from Uppsala, Sweden, Geografiska Annaler: Series A," *Phys. Geogr.*, vol. 87, no. 4, pp. 539–548, 2005.

Kashif Mahmud was born in Dhaka, Bangladesh, in 1984. He received the B.Sc. and M.Sc. degrees in civil engineering from Bangladesh University of Engineering and Technology, Dhaka, Bangladesh, in 2007 and 2010, respectively. Since 2012, he has been pursuing the Ph.D. degree in hydrogeology at the Connected Waters Initiative Research Centre, University of New South Wales Australia, Sydney, N.S.W., Australia.

From 2010, he was an Assistant Professor with the Department of Civil and Environmental Engineering, Islamic University of Technology, Board Bazar, Bangladesh. He has authored 13 journal articles and has presented in 16 national and international conferences. His research interests include multiple point geostatistics, characterizing subsurface heterogeneity, and karst hydrogeology.

Gregoire Mariethoz was born in Neuchâtel, Switzerland, in 1978. He received the M.S., MAS, and Ph.D. degrees in hydrogeology from the University of Neuchâtel, Neuchâtel, Switzerland, in 2003, 2006, and 2009, respectively.

From 2009 and 2010, he was a Postdoctoral Researcher with Stanford University, Stanford, CA, USA, and between 2010 and 2014, he was a Senior Lecturer with the University of New South Wales Australia, Sydney, N.S.W., Australia. Since 2014, he has been an Assistant Professor with the University of Lausanne, Lausanne, Switzerland. His research interests include the development of spatial statistics algorithms and their application in hydrology, hydrogeology, and remote sensing.

Pauline C. Treble received the B.Sc. degree (Hons.) in physical geography from the University of Sydney, Sydney, N.S.W., Australia, in 1998, and the Ph.D. degree in quaternary science from the Australian National University, Canberra, A.C.T., Australia, in 2003.

From 2004 to 2005, she was a Postdoctoral Researcher with the School of Earth, Planetary and Space Sciences, University of California Los Angeles, Los Angeles, CA, USA, and from 2005 to 2008, was a Research Fellow with the Research School of Earth Sciences, Australian National University. Since 2008, she has been a Research Scientist with the Institute for Environmental Research, the Australian Nuclear Science and Technology Organisation, Lucas Heights, N.S.W., Australia. Her research interests include speleothem paleoclimatology.

Andy Baker was born in Romford, England, in 1968. He received the B.Sc. and Ph.D. degrees in geographical science from the University of Bristol, Bristol, U.K., in 1990 and 1993, respectively.

From 1993 to 1998, he was employed with the University of Exeter, Exeter, U.K., from 1998 to 2003, with the University of Newcastle-upon-Tyne, Newcastle upon Tyne, U.K., and from 2003 to 2009, with the University of Birmingham, Birmingham, U.K.. Since 2010, he has been employed with the University of New South Wales Australia, Sydney, N.S.W., Australia. He is currently the Director of the Connected Waters Initiative Research Centre. He has coauthored the book *Speleothem Science* (Wiley-Blackwell, 2012). His research interests include karst hydrogeology, geochemistry, and the reconstruction of past climate records from speleothems.